

Non-equilibrium heating path for the laser-induced nucleation of metastable skyrmion lattices

P. Olleros-Rodríguez,* M. S. Strungaru, S. I. Ruta, P. I. Gavriloea,* A. Gudín, P. Perna, R. W. Chantrell, O. Chubykalo-Fesenko

*Corresponding authors: pablo.olleros@imdea.org

paul.gavriloea@csic.es

1. Curie Temperature

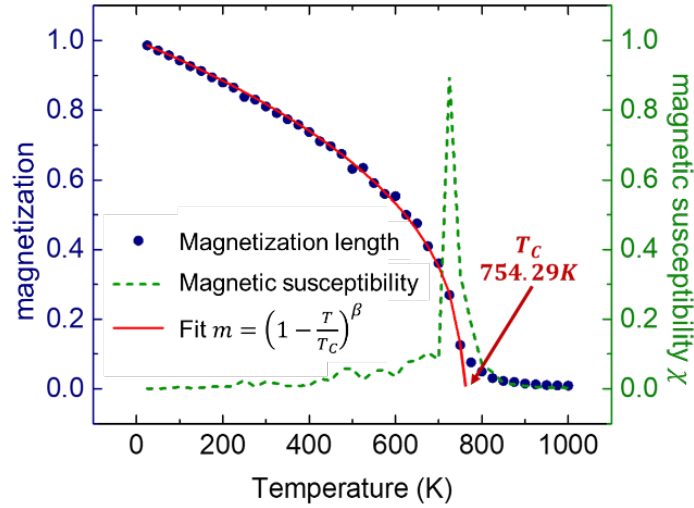


Fig. S1. Curie Temperature (T_C). The T_C is obtained by fitting (red solid line) the simulated dependence of the reduced magnetization m (blue dots). The divergence of the magnetic susceptibility χ (green dashed lines) takes place in the transition from the ferromagnetic to the paramagnetic state.

We obtained the Curie Temperature of the system T_C by reproducing the reduced magnetization $m=M/M_S$ (being M_S the saturation magnetization) dependence with the temperature T . The Dzyaloshinskii-Moriya Interaction (DMI) (having negligible influence on T_C) is deactivated in this case as it produces the nucleation of labyrinth domains with no net magnetisation. The simulation starts from an initial saturated state pointing along the positive out-of-plane direction (i.e. $m_z = +1$) increasing the temperature in steps of $\Delta T = 25K$ and equilibrating the system at each temperature by solving the stochastic LLG equation with a time step $\Delta t=10^{-16}$ s during 100ps. After the initial equilibration stage, the magnetization is averaged over 100ps. In Fig. S1, the averaged magnetization m (blue dots) is plotted versus temperature T . The Curie temperature T_C is obtained by fitting (red solid line) the resulting curve to the following expression:

$$m(T) = \left(1 - \frac{T}{T_C}\right)^\beta$$

giving $T_C = 754.29$ K and $\beta = 0.39$ for the considered 3 monolayers of hcp-Cobalt system. The susceptibility of the system (green dashed line) is calculated as following:

$$\chi_{\alpha} = \frac{\mu_i}{k_B T} (\langle m_{\alpha}^2 \rangle - \langle m_{\alpha} \rangle^2); \quad m_{\alpha} = m_x, m_y, m_z, |m|$$

The divergence point of susceptibility associated to the ferromagnetic to paramagnetic phase transition agrees with the fitted Curie Temperature.

2. Configurations of nucleated skyrmion lattices

In order to explore the character of the nucleated skyrmion lattices, we have conducted atomistic simulations in which a skyrmion lattice was obtained after the application of a laser pulse of fluence $F_0 = 5.6 \text{ mJ/cm}^2$ and duration $t_p = 50 \text{ fs}$. The three magnetisation components at 300 K are presented in Fig. S2 (upper row). To have a better visualisation of the lattice, it was further cooled down towards a final temperature $T = 0 \text{ K}$ during 2 ns and in the absence of external fields, see Fig. S2 (lower row).

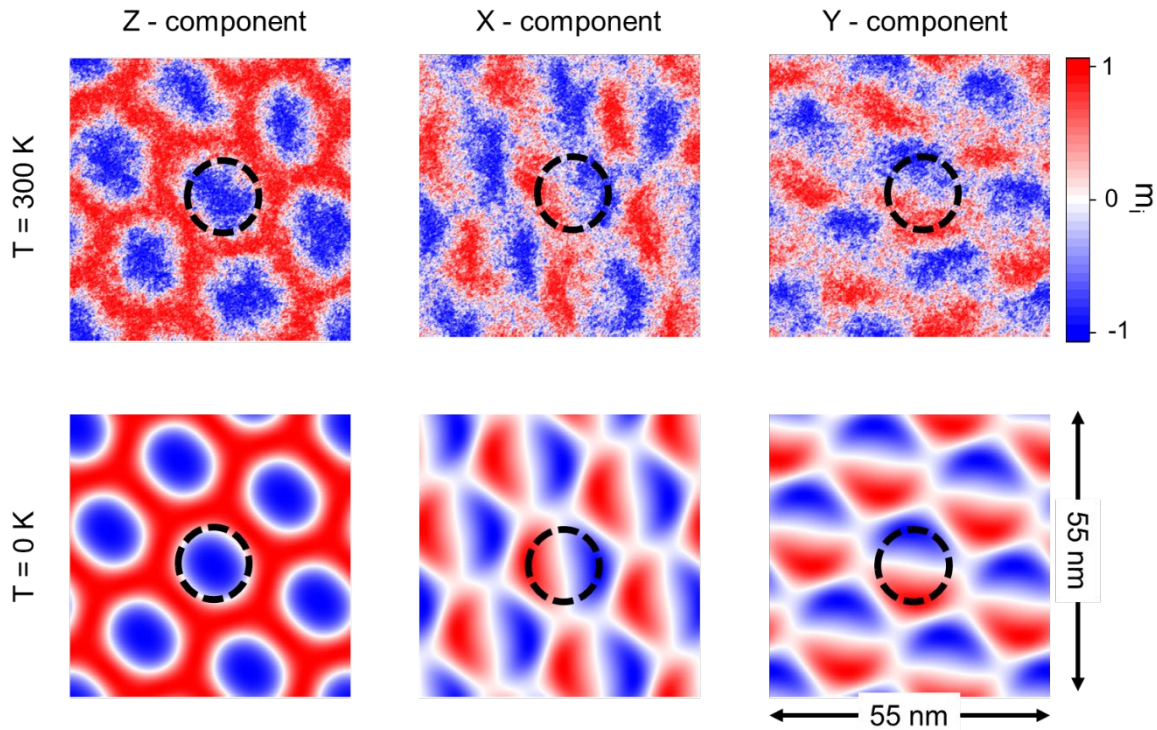


Fig. S2 Spin configuration of a skyrmion lattice in the absence of external fields. The initial skyrmion lattice at 300 K (top row) was obtained after the application of a laser pulse with fluence $F_0 = 5.6 \text{ mJ/cm}^2$ and $t_p = 50 \text{ fs}$, and subsequently cooled down during 2 ns in the absence of an external field towards a final temperature of $T = 0 \text{ K}$ (bottom row). From left to right, the columns represent the Z-, X- and Y- components of the magnetization. The dashed circle is included to facilitate the interpretation.

Focusing on the dashed circles included in the images, the chiral character can be deduced. The results reveal that the nucleated skyrmions share the same Néel clockwise chiral character defined by the sign of the DMI. In Fig. S3 we show the magnetization components of two skyrmion lattices that were nucleated after following the application of a laser pulse of fluence $F_0 = 8 \text{ mJ/cm}^2$ and pulse length $t_p = 50 \text{ fs}$ and under external fields $B_{\text{app}} = 2 \text{ T}$ (top row) and $B_{\text{app}} = -2 \text{ T}$ (bottom row).

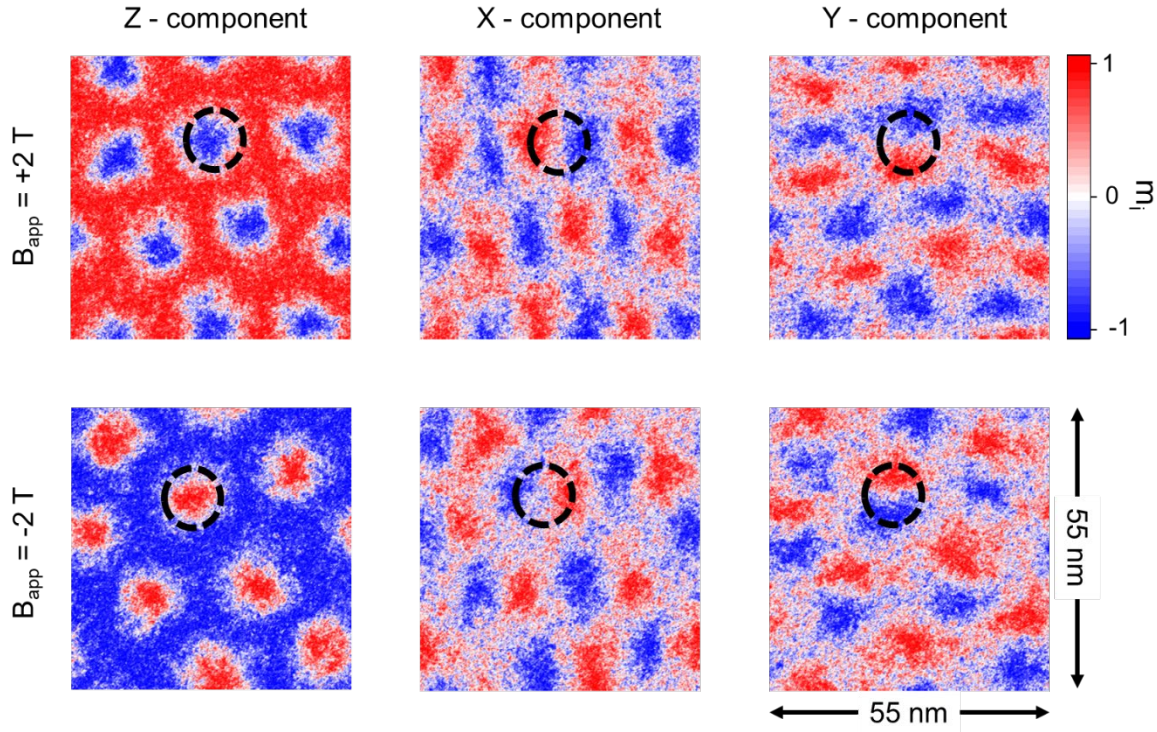


Fig. S3. Spin configuration of a skyrmion lattice under the influence of external fields $B_{\text{app}} = 2 \text{ T}$ (top row) and $B_{\text{app}} = -2 \text{ T}$ (bottom row). From left to right, the columns represent the Z-, X- and Y- components of the magnetization. The dashed circle is included to facilitate the interpretation.

The skyrmion lattices share the same chirality, also when both polarizations of the skyrmions are obtained. As it can be seen in Fig. S3, the in-plane components of the magnetization change their sign when the skyrmion polarity is reversed. Indeed, the colors' pattern in the dashed circle changes and the chirality is conserved.

3. Influence of magnon localization and magnon coalescence on skyrmion nucleation

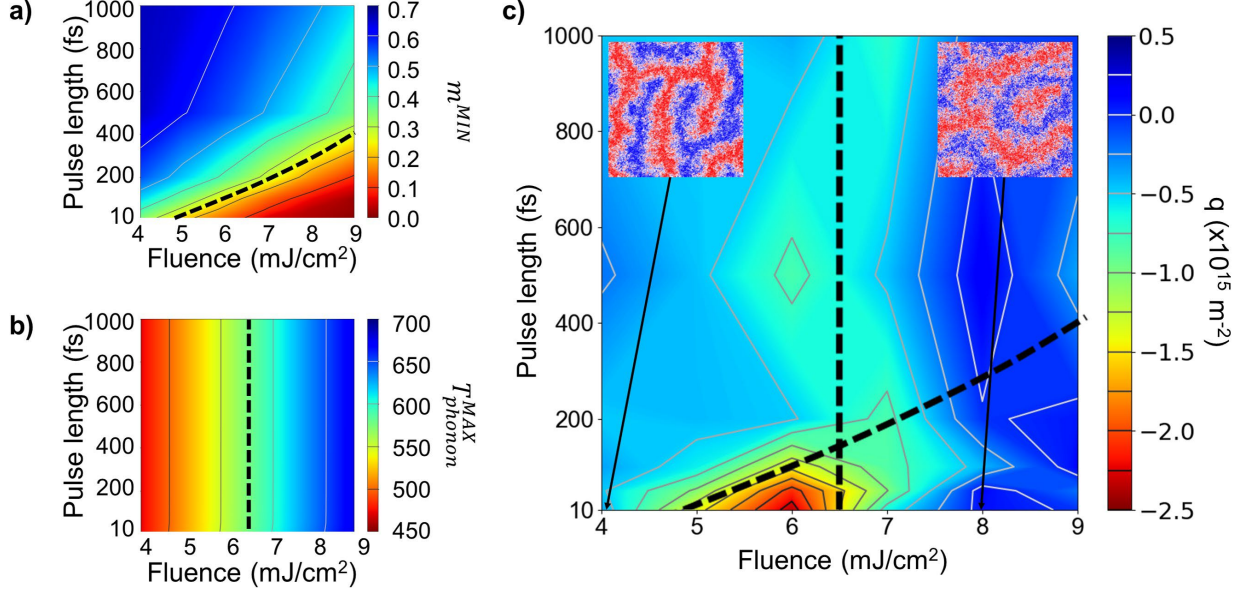


Fig. S4. Influence of demagnetization and equilibration temperature in the nucleation of skyrmion lattices. (a) Minimum magnetization reached after the laser pulse is applied depending on the laser pulse parameters. The dashed line represents a constant value $m^{MIN} \sim 0.25$. (b) Final phonon temperature (when equilibrated with the electrons) depending on the laser pulse parameters. The dashed lines represent a constant equilibration temperature $T^{MAX}_{phonon} \sim 580$ K. (c) Phase diagram of the topological charge density. The dashed lines are transferred from panels a) and b). The insets show obtained labyrinth-like domains obtained at $t_p = 10$ fs and different fluences.

The influence of the magnon localization process and the quasi-equilibrium phonon-electron temperature on the nucleation of skyrmion lattices can be seen in Fig. S4. In panel a) we show the minimum magnetization reached by the system after the laser pulse is applied. In panel b) we present the final quasi-equilibrium phonon-electron temperature due exclusively to the effect of the laser. The far from equilibrium nature of the magnon localization process requires a large level of demagnetization in order to nucleate a larger number of magnon drops. On the other hand, and during the magnon coalescence phase, the thermal fluctuation affects the achievement of topological protection, and the final equilibrium temperature (that matches the maximum temperature reached by the phononic subsystem) should not overcome a certain value to allow the protection of the domains. In panels a) and b) the dashed black lines represent a constant minimum magnetization of m^{MIN} and a constant equilibrium temperature of $T^{MAX}_{phonon} \sim 580$ K respectively. If we transfer these lines to the computed phase diagram of the topological charge density (Panel c) it can be observed that the region of interest in which the skyrmion lattices are

nucleated is well delimited within the lines. Thus, it can be interpreted that for fluences $F_0 > 6.5$ mJ/cm², the high temperatures reached by the system prevents the topological protection of the magnetic domains and they merge into larger and labyrinthine-like domains (see right inset in Panel c). For fluences $F_0 < 6.5$ mJ/cm² if the minimum magnetization is above $m^{MIN} > 0.25$ we are not demagnetizing the system enough to promote the nucleation of a sufficient number of magnon drops and only a few of them appear and grow later to large and labyrinth-like domains (see left inset in Panel c).

4. Ground States under applied field

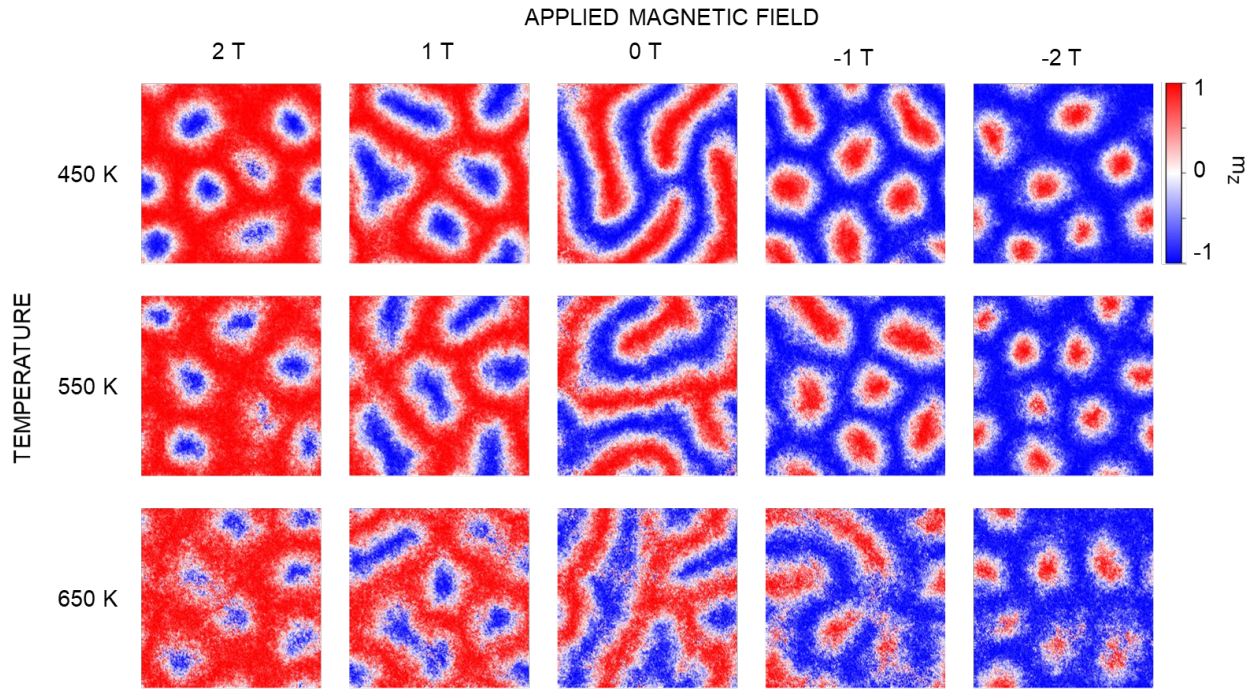


Fig. S5. Final magnetic configurations after following field cooling processes from the paramagnetic state.

The ground states of the system under different applied fields were obtained following field-cooling processes as described in Methods. Fig. S5 shows selected magnetic configurations of the obtained ground states at different final temperatures and under different applied external fields. To reduce the thermal noise, the presented configurations were averaged over the last 100 ps of the simulation.

5. Magnon localization at high fields

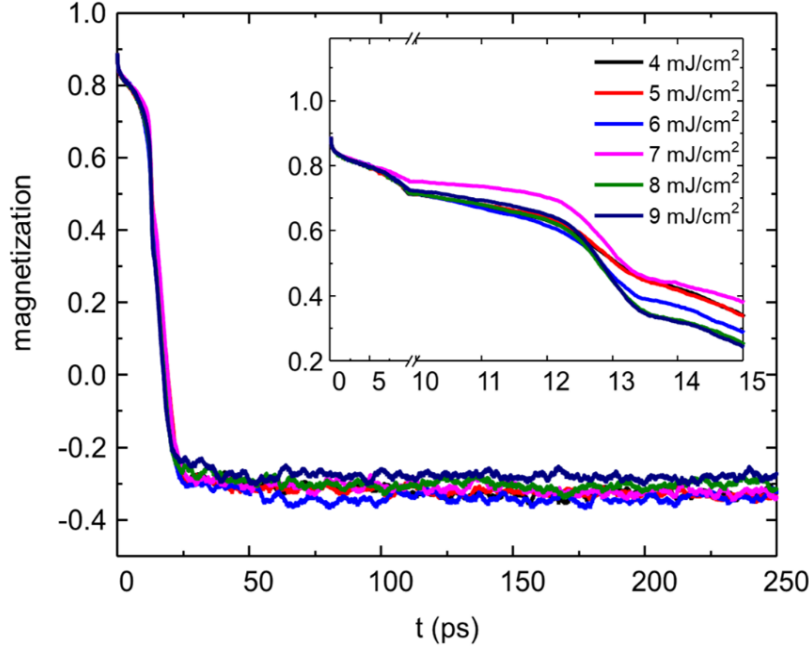


Fig. S6. Magnon localization at -2T and 1000 fs pulse lengths. Magnetization profiles following the application of a laser pulse with a pulse length $t_p = 1000$ fs and under an external field of -2T. The region covering the first 15 ps is plotted in the inset. The inflection points at $t \sim 13.5$ ps is related to the beginning of the magnon localization process.

In Fig. S6 we present the magnetization profiles when $t_p = 1$ ps and when an external field of $B_{app} = -2T$ is applied. The inflection point in the inset of Fig. S6 reveals that the magnon localization process takes place even in the presence of strong external fields. In contrast, a smooth transition would reveal an adiabatic process in which the system follows a quasi-equilibrium path along the spin configuration space.

6. Skyrmion sizes

The skyrmion radii are computed by assuming an almost circular shape and neglecting the domain wall widths in comparison to the skyrmion sizes. The reduced magnetization is related to the area of the sample with magnetization pointing upwards (downwards) A^\uparrow (A^\downarrow) by

$$m = \frac{A^\uparrow - A^\downarrow}{A^\uparrow + A^\downarrow} = 1 - \frac{2A^\downarrow}{A}$$

; where $A = A^\uparrow + A^\downarrow$ is the total area of the sample. In a sample populated with skyrmions whose cores are pointing downwards i.e. the negative values of the OOP direction

$A^\downarrow = N_{sk} \pi R_{sk}^2 = A n_{sk} \pi R_{sk}^2$. The magnetization is thus related to the skyrmion density as $m = 1 - 2n_{sk} \pi R_{sk}^2$. The latter relation can be generalized as $m = -P_{core} + 2n_{sk} P_{core} \pi R_{sk}^2 = -\frac{q}{|q|} + 2q\pi R_{sk}^2$. This allows us to approximately evaluate the average skyrmion size from magnetization. The radii values have been averaged over various sets of simulations.

Fig. S7 shows the dependence of the computed skyrmion radii obtained under application of the laser pulse with 50 fs duration (filled symbols) and FCP in the cases when 6 skyrmions (Panel a) and 7 skyrmions (Panel b) are nucleated within the simulated area (i.e. a $55 \text{ nm} \times 55 \text{ nm}^2$ thin film). For illustrative purposes, linear fits of the light-induced nucleated skyrmion radii have been added (dashed lines). As expected, the skyrmion radius decreases with increasing external applied fields. Note the background magnetization switching for 2 T applied field (i.e. the magnetization outside skyrmions has switched to the negative direction – see Fig. 4.d in main text). In agreement with predictions of Tomasello *et al.*,¹ skyrmion radius also increases with temperature and the slope of the in-field dependence is higher than at zero field, indicating the transition from metastable to stable skyrmions.

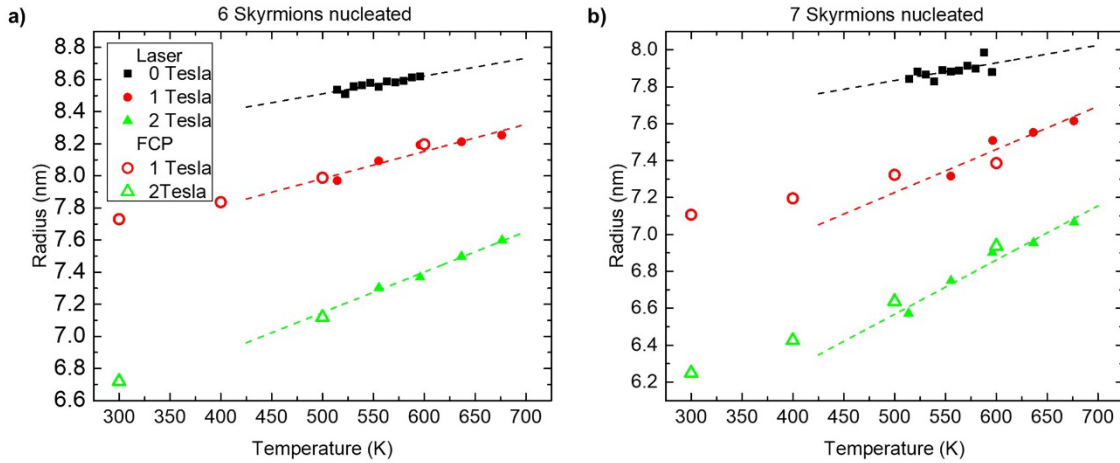


Fig. S7. Skyrmion radius vs temperature. Skyrmions are nucleated under laser pulse with duration 50 fs (filled symbols) and under the field-cool protocol (empty symbols) with and without applied field. In the case of the laser excitation, the temperature corresponds to quasi-equilibrium temperatures. **(a)** Skyrmion radius when 6 skyrmions are nucleated within the sample (i.e. $q = 1.98 \times 10^{15} \text{ m}^{-2}$). **(b)** Skyrmion radius when 7 skyrmions are nucleated within the sample (i.e. $q = 2.31 \times 10^{15} \text{ m}^{-2}$). The dashed lines are linear fits added for illustrative purposes.

Our first observation is related to the fact that the skyrmion radius depends on the number of nucleated skyrmions due to the finite size of the modelled system. This confinement effect may happen also in the experimental situation due to the finite size of the laser spot. Secondly, while during the laser-induced nucleation we got from 4 to 10 nucleated skyrmions, in the FCP simulations we obtained a smaller dispersion in their number (from 6 to 8). We also observe that in the case of 6 nucleated skyrmions the radii obtained with both protocols match perfectly which is not the case of 7 nucleated skyrmions. The difference between equilibrium and non-equilibrium radii is even more pronounced for other skyrmion numbers. This difference might arise due to the

high temperatures and the fluctuations of the topological charge. But more importantly it reflects the fact that the number of skyrmions in the laser-induced process depends on the MDs nucleation and their survival rather than on the equilibrium skyrmion radius which for $B_{app} = 1$ T corresponds to 6 skyrmions as is shown in Fig. 5 of the main text.

7. Micromagnetic simulations of the skyrmion lattice

Longer -time and larger -scale simulations have been performed using the computational code MuMax3.² Additionally, this allowed us to study the effect of the demagnetizing field on the stabilization of the skyrmion lattices.

The relation between atomistic and micromagnetic parameters is not trivial and depends on the crystal structure and the nature of the interface. At zero temperatures the micromagnetic exchange stiffness A_{ex} was evaluated from the atomistic parameter J for the hcp lattice following Moreno *et al.*³ For the micromagnetic DMI parameter D_{Ind} we assumed the atomistic relation $J/D = 10$ that in the micromagnetic framework gives the relation $A_{ex}/(D_{Ind} \cdot t_{Co})$. Micromagnetic approach also requires macroscopic temperature-dependent parameters. While the saturation magnetization can be directly transferred from the atomistic to the micromagnetic framework, other temperature dependencies are not trivial. They are typically expressed in terms of the power laws of the temperature dependent magnetisation. We will assumed the following scaling relations for the micromagnetic parameters: $A_{ex}(T) \sim m(T)^{1.8}$ (see Moreno *et al.*³); $K_U(T) \sim m(T)^3$ (the Callen-Callen law for uniaxial magnets). The temperature-scaling of the macroscopic DMI is not well known for ultra-thin films and we fitted this parameters assuming the same skyrmion size as in the atomistic approach.

The final list of micromagnetic parameters used in the present series of micromagnetic simulations are as follows:

Table S1. Temperature dependent re-scaled, micromagnetic parameters.

	Atomistic	Micromagnetic @ 0 K	Micromagnetic @ 300 K
Saturation Magnetization	$\mu_S = 1.61\mu_B$	$M_S = 1.35$ MA/m	$M_S = 1.11$ MA/m
Direct Exchange	$J = 4.8e-21$ J/atom	$A_{ex} = 14.8$ pJ/m ³	$A_{ex} = 10.4$ pJ/m ³
DMI	$D = 4.8 e-22$ J/atom	$D_{Ind} = 9$ mJ/m ²	$D_{Ind} = 6.3$ mJ/m ²
Magnetic anisotropy	$K_U = 5.85e-24$ J/atom	$K_U = 0.53$ MJ/m ³	$K_U = 0.29$ MJ/m ³

It must be noted that the uniaxial anisotropy used in the atomistic study included the shape anisotropy. Thus, when the long range dipolar interactions are introduced in the code, the uniaxial anisotropy of the system must be corrected by $K_U^{(\text{Demag ON})} = K_U^{(\text{Demag OFF})} + K_{\text{shape}}$ which at 0 K results in $K_U^{(\text{Demag On})} (T = 0 \text{ K}) = 1.68 \text{ MJ/m}^3$.

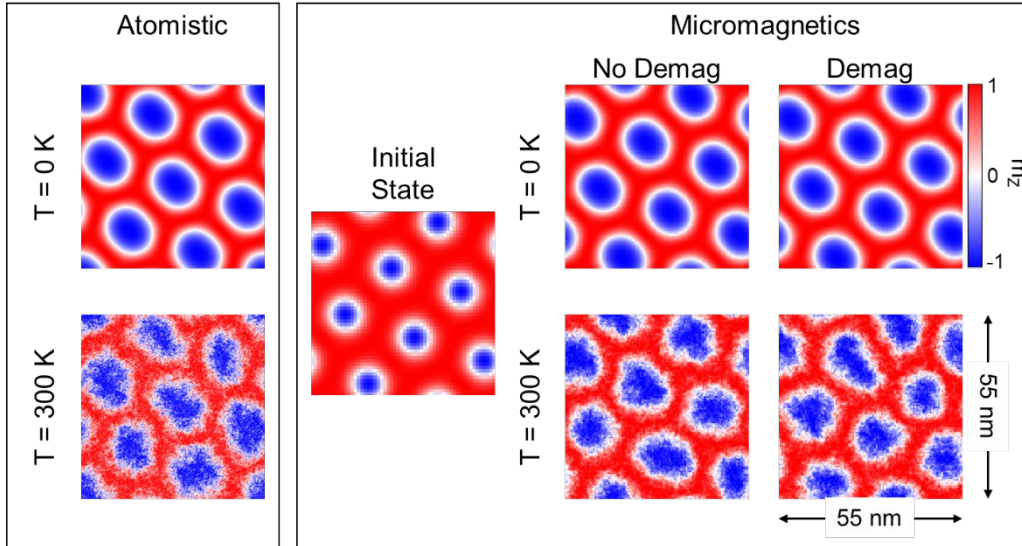


Fig. S8. Comparison between atomistic and micromagnetic simulations at 0 and 300K. “No Demag” means that the magnetostatic interactions are included into the renormalized anisotropy constant and the direct magnetostatic interactions are switched off.

First we have studied the stability of skyrmion lattices in comparison with the atomistic calculations. We used a 55 nm x 55 nm x 0.41 nm cobalt thin film with periodic boundary conditions (PBC). The results are shown in figure S8. In the left box we show, for reference purposes, the skyrmion lattice obtained via atomistic calculations after the application of a laser pulse with fluence $F_0 = 5.6 \text{ mJ/cm}^2$ and pulse width $t_p = 50 \text{ fs}$ and subsequently cooled the system down to 0 K. In the right box we show the resulting micromagnetic simulations after an initial state of a skyrmion lattice (as shown in the figure) is equilibrated by solving the LLG equation during 5 ns. The simulations were carried out without (left column) the dipolar interactions (and with renormalized anisotropy constant) and with them (without the renormalized constant), and at $T = 0 \text{ K}$ (upper row) and at $T = 300 \text{ K}$ (bottom row). In the simulations at $T = 300 \text{ K}$, apart from the scaled parameters, we have introduced thermal fluctuations.

Next we tried to reproduce the situation in which a skyrmion lattice is nucleated in a center of a large thin film. The simulated system have $512 \times 512 \text{ nm}^2$ without considering PBC. Results of the simulations are summarized in figure S9. The initial state is represented by a magnetic configuration close to a hexagonal skyrmion lattice. It was equilibrated at $T = 0 \text{ K}$ and $T = 300 \text{ K}$ by solving the LLG equation during 5 ns. The results reveal that those skyrmions placed at the edge of the skyrmion lattice, tend to increase their size and they expand by forming labyrinth-like domains that limit the growth of the skyrmions placed in the core of the inner part of the lattice. Thus, in this situation, the surviving skyrmions are constrained due to the effect of the surrounding

stripe domains, even in the absence of PBC. As a result of the constraint, we do not observe a large variation on both the size and the separation of the surviving skyrmions.

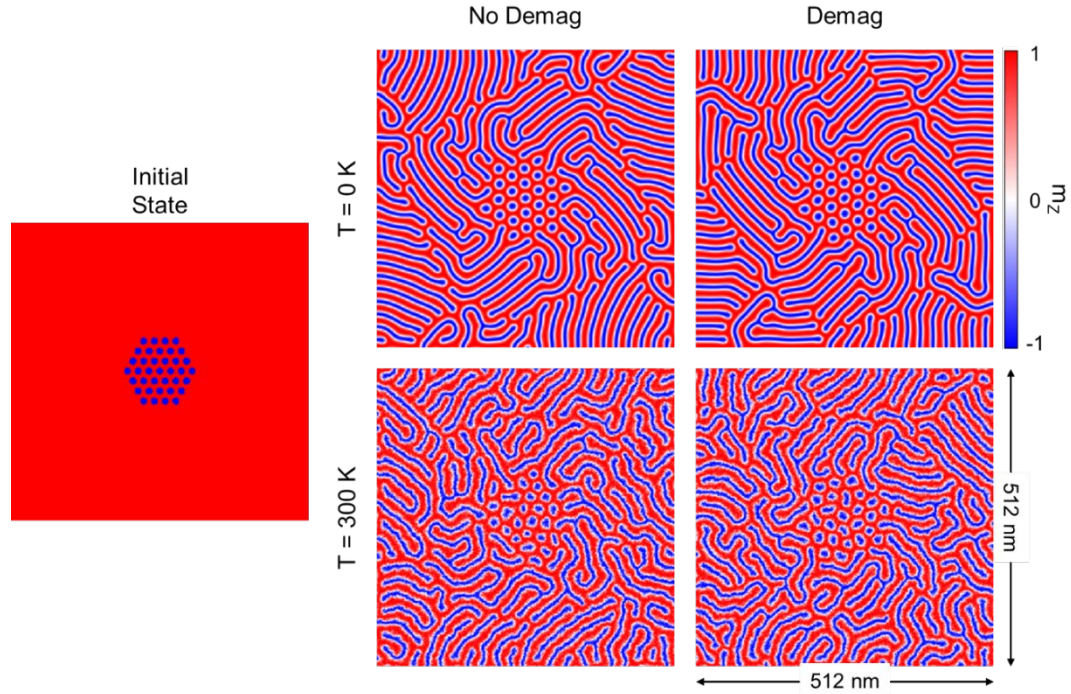


Fig. S9. Micromagnetic simulations. The results are shown after placing the skyrmion lattice in the sample center and after solving Langevin dynamics during 5 ns.

References

1. R. Tomasello, K. Y. Guslienko, M. Ricci, A. Giordano, J. Barker, M. Carpentieri, O. Chubykalo-Fesenko, G. Finocchio, *Phys. Rev. B*, 97(6), 060402 (2018)
2. A. Vansteenkiste, J. Leliaert, M. Dvornik, M. Helsen, F. Garcia-Sanchez, B. Van Waeyenberge, *AIP Adv.*, 4(10), 107133 (2014)
3. R. Moreno, R. F. L. Evans, S. Khmelevskiy, M. C. Muñoz, R. W. Chantrell, O. Chubykalo-Fesenko, *Phys. Rev. B*, 94(10), 104433 (2016).